3-D Ultrasound Imaging Using a Forward-Looking CMUT Ring Array for Intravascular/Intracardiac Applications

David T. Yeh, *Student Member, IEEE*, Ömer Oralkan, *Member, IEEE*,
Ira O. Wygant, *Student Member, IEEE*, Matthew O'Donnell, *Fellow, IEEE*,
and Butrus T. Khuri-Yakub, *Fellow, IEEE*

Abstract—Forward-viewing ring arrays can enable new applications in intravascular and intracardiac ultrasound. This work presents compelling, full-synthetic, phased-array volumetric images from a forward-viewing capacitive micromachined ultrasonic transducer (CMUT) ring array wire bonded to a custom integrated circuit front end. The CMUT ring array has a diameter of 2 mm and 64 elements each 100 μm $\times$ 100 μm in size. In conventional mode, echo signals received from a plane reflector at 5 mm had 70% fractional bandwidth around a center frequency of 8.3 MHz. In collapse mode, 69% fractional bandwidth is measured around 19 MHz. Measured signal-to-noise ratio (SNR) of the echo averaged 16 times was 29 dB for conventional operation and 35 dB for collapse mode. B-scans were generated of a target consisting of steel wires 0.3 mm in diameter to determine resolution performance. The 6 dB axial and lateral resolutions for the B-scan of the wire target are 189 μm and 0.112 radians for 8 MHz, and 78 μm and 0.051 radians for 19 MHz. A reduced firing set suitable for real-time, intravascular applications was generated and shown to produce acceptable images. Rendered three-dimensional (3-D) images of a Palmaz-Schatz stent also are shown, demonstrating that the imaging quality is sufficient for practical applications.

I. Introduction

FORWARD-viewing intravascular ultrasound (IVUS) enables new procedures in cardiac medicine such as viewing severely occluded blood vessels, guiding stent placement, and monitoring ablation operations in the heart. A forward-viewing transducer for catheter-based applications requires clearance in the center of the transducer for the guidewire. This motivates the development of a ring array. A ring-shaped aperture also is capable of volumetric imaging, which reduces operator dependence in clinical ultrasound and enables new modes of visualization. A thorough discussion of forward-viewing IVUS, including a listing of single-element transducers and arrays in the literature, is found in [1].

TABLE I
PHYSICAL PARAMETERS OF CMUT RING ARRAY.

Number of elements	64
Ring diameter, mm	2
Element pitch, μm	102
Element size, μm^2	100×100
Cells per element	9
Cell radius, μm	13
Membrane thickness, μm	0.4
Electrode radius, μm	9.0
Metal electrode thickness, μm	0.3
Gap distance, μm	0.15
Silicon substrate thickness, μm	500

Although a ring array provides the geometry required for IVUS, a straightforward approach at beamforming with such an aperture results in compromised resolution. To address this, a weighting scheme that achieves full disk-aperture resolution from an infinitesimally thin ring was reported in [2], [3]. Later work studied weighting methods for rings with finite radial extent [4] and a reduced firing set to achieve a frame rate suitable for IVUS [1].

Previous efforts have found it challenging to design and fabricate piezoelectric transducers of the dimensions required for forward-looking ring arrays [5]. The image quality was not sufficient to be of clinical value because of low element yield. There have been several efforts to make ring arrays using capacitive micromachined ultrasonic transducers (CMUTs) for the purpose of volumetric intravascular ultrasound [6]–[11].

This paper presents characterization of a CMUT ring array coupled to custom integrated circuits and compelling volumetric, synthetic, phased-array images that demonstrate the utility of such a device.

A. Capacitive Micromachined Ultrasonic Transducers

A CMUT array is composed of elements like any piezoelectric array. Each element, however, is composed of several cells, or membranes (Fig. 1), the design of which determine the operating characteristics of the transducer, such as frequency, bandwidth, sensitivity, and optimum bias voltage. The parameters of the CMUT ring array used in this study are given in Table I.
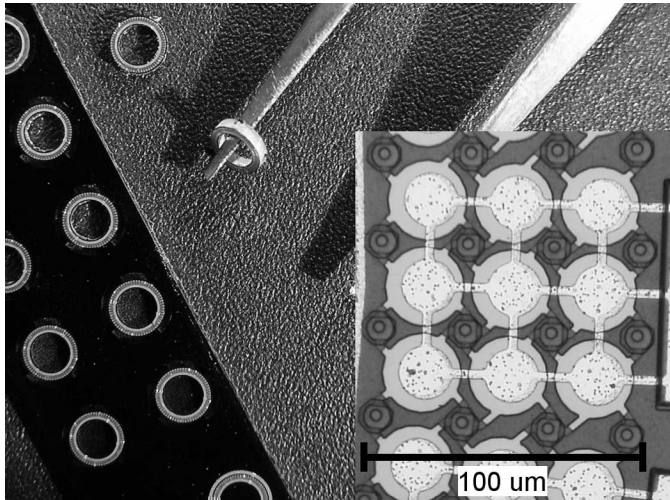
Fig. 1. Background, several ring arrays from a single wafer with centers removed. Right, 3×3 cell structure of a single CMUT element.

Fig. 2. Simulated angular response: comparison between CMUT and rectangular element at the same frequency.

CMUTs have several advantages over piezoelectric transducers for medical imaging [12]. Microlithography is used to pattern the features that compose a CMUT and routinely yields the small dimensions required for ring arrays. Fig. 1 illustrates the batch fabrication capability of the CMUT manufacturing process and the ability to remove the centers of the rings. Array elements can be made very small easily and very close together. The cell structure of CMUTs naturally decouples operating frequency from transducer-element size, which is crucial because ring-array elements are typically small. The wide bandwidth of CMUTs in immersion improves the resolution of ultrasound images. In addition, this transducer covers a frequency range from 4 MHz to 25 MHz, including both conventional and collapse modes. This wide range allows a variety of imaging schemes.

In contrast to the piezo transducer, the CMUT typically requires a direct current (DC) bias for operation. One should note, however, that the bias is not a power source but merely a static charge to deflect the CMUT membrane; therefore, high currents and power are not necessary. Furthermore, the bias would be applied on the side of the CMUT internal to the catheter, and all surfaces exposed to the patient would be grounded.

The CMUT features a collapse mode operation that has particularly good characteristics for imaging, including higher echo signal levels and higher frequencies [8], [13]. The option of a collapse mode makes it possible during the imaging procedure to switch between two modes with different characteristics. The operator can choose conventional, lower frequency operation for better penetration to navigate, or collapse mode, higher frequency operation for higher resolution to make a diagnosis.

B. Angular Response

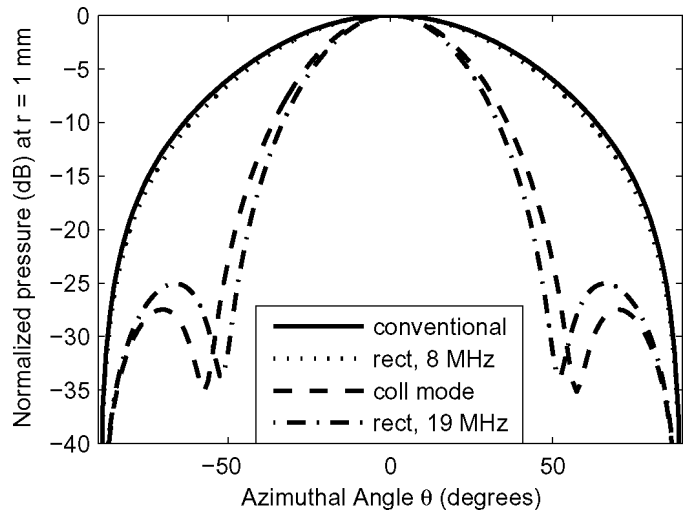The cell structure of the CMUT may cause one to question whether this affects the angular response of the trans-

ducer element. Fig. 2 compares the computed angular response of a CMUT in conventional and collapse modes to that of an ideal, rectangular transducer element. Each angular response curve was computed by fitting the transducer's displacement profile to a 2-D grid and numerically performing the Rayleigh-Sommerfeld integral for a pressure release baffle [14].

Each CMUT cell has a circularly symmetric displacement profile. Therefore, the radial variation for conventional operation is approximated by the first quarter cycle of a cosine. Collapse mode operation has fixed displacement in the center; thus, the radial variation is approximated by the first half cycle of a sine with double the radial frequency of the cosine of conventional operation. Nine cells are laid out in a 3×3 square with 31 μm separation between cell centers.

These calculations show that the cell structure has a minimal effect on the angular response of the transducer. The difference between the rectangular element and the CMUT lies mainly in the size of the element. The rectangular element is 100 μm $\times$ 100 μm, whereas a box outlining the active area of the CMUT is 88 μm $\times$ 88 μm.

II. EXPERIMENTAL SETUP

A data acquisition system was developed to collect A-scans from the 64 elements of the ring array. For prototyping purposes, this system used full-synthetic, phased-array imaging to acquire a complete data set so that various beamforming approaches could be evaluated offline. Elements were excited one at a time, and A-scans were acquired from the entire array for each transmit element using a digitizing oscilloscope (Infinium 54825A, Hewlett-Packard Co., Palo Alto, CA). Each A-scan was collected at a sampling rate of 500 MS/s for both conventional and collapse modes, averaged 16 times.

A custom integrated circuit (IC) [9], developed to interface with high-frequency CMUTs for testing purposes,
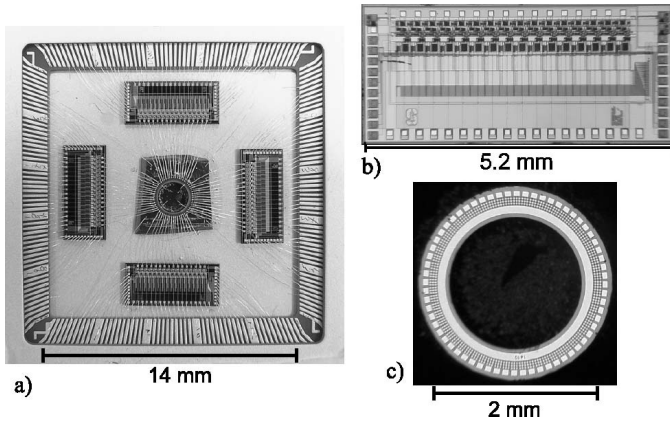
Fig. 3. (a) Ring-array wire bonded to electronics. (b) 16-channel transmit/receive circuit. (c) 64-element CMUT ring array with hole in the center.

was used to minimize capacitive parasitics that would otherwise greatly attenuate the signal from the tiny ring array element. Each IC is 5.2 mm × 2.3 mm in size, and includes 16 independent channels of pulser/receiver circuitry. Four IC chips were wire bonded to the 64 elements of the CMUT in a 209 pin grid array (PGA) electronics package, as shown in Fig. 3(a).

Vegetable oil was used as the acoustic medium for imaging experiments because it provides isolation between the electrical nodes in the package (bond wires, ICs, CMUT). However, the attenuation of sound in oil increases with frequency more rapidly than it does in water [12], resulting in a pessimistic estimate of the SNR for the higher frequency experiments.

III. RESULTS

A. A-Scan Results

Pulse-echo data of a plane reflector, the oil-air interface, at 5 mm were averaged 16 times and acquired for all 64×64 transmit-receive combinations using a 25 V unipolar pulse as the excitation. For the conventional case (30 V DC bias), the pulse width was 60 ns; for collapse mode (100 V DC bias), the pulse width was 27 ns. These pulse widths were found experimentally to maximize the amplitude of the echo signal. This roughly sets the first zero of the pulse in the frequency domain to be twice the center frequency of the transducer.

Fig. 4 shows the echo signal from a typical array element and exhibits the wide bandwidth of the CMUT. The main pulse lasts 1.5 to 2.5 cycles and is followed by a ringing tail. The tail is the result of cross talk and is greatly reduced in collapse mode [15]. The average SNR over all 64 array elements for this plane reflector is 29 dB for conventional operation and 35 dB for collapse mode. The calculated loss due to attenuation and diffraction for a 100 μm×100 μm square aperture at the frequencies of conventional and collapse modes is 49 dB and 57 dB, respectively.
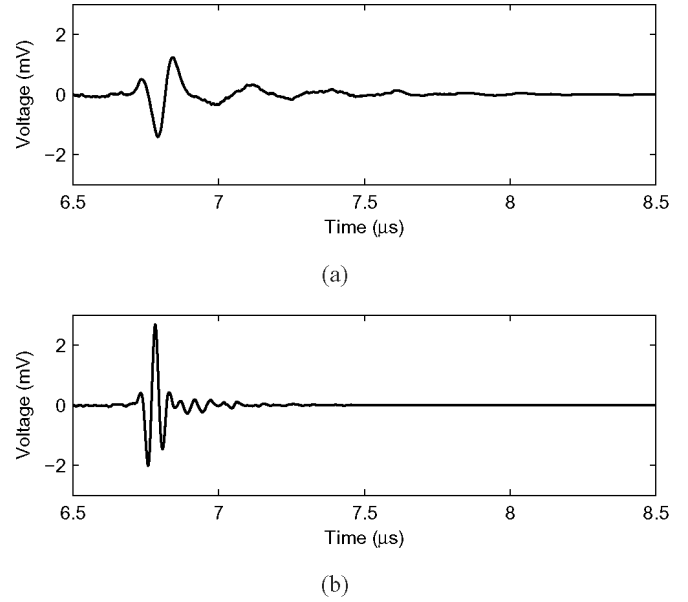

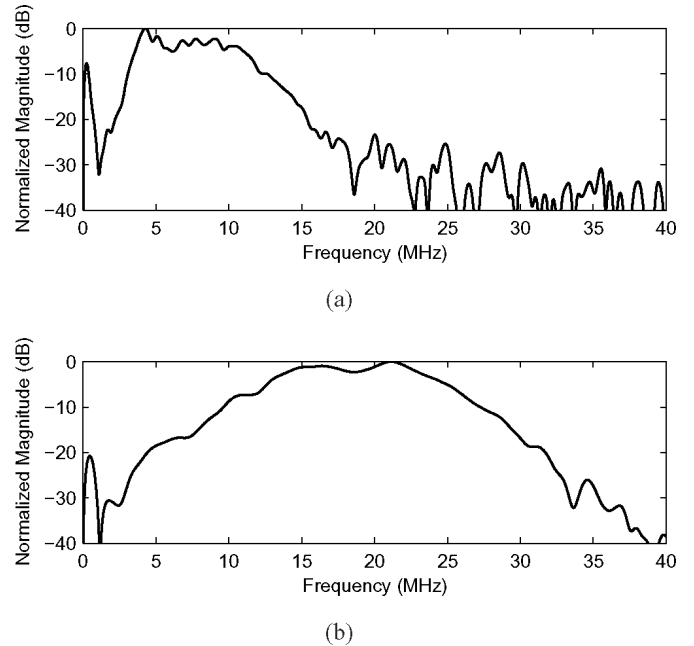Fig. 4. Pulse-echo response. (a) Conventional. (b) Collapse mode.

Fig. 5. FFT of pulse-echo response. (a) Conventional. (b) Collapse mode.

Fig. 5 shows the fast Fourier transform (FFT) of the unfiltered pulse-echo signal, and Fig. 6 shows the FFT of this signal after it has been filtered for imaging. The imaging filter was a 300-tap Gaussian-window bandpass finite impulse response (FIR) filter with $\alpha = 2.5$. For conventional mode, the filter had a 6 dB passband from 5.5 to 13 MHz. For collapse mode, the filter had a 6 dB passband from 10 to 27.5 MHz.

Using the filtered data, the center frequencies, and fractional bandwidths of all 64 elements were calculated according to the following definitions: center frequency:

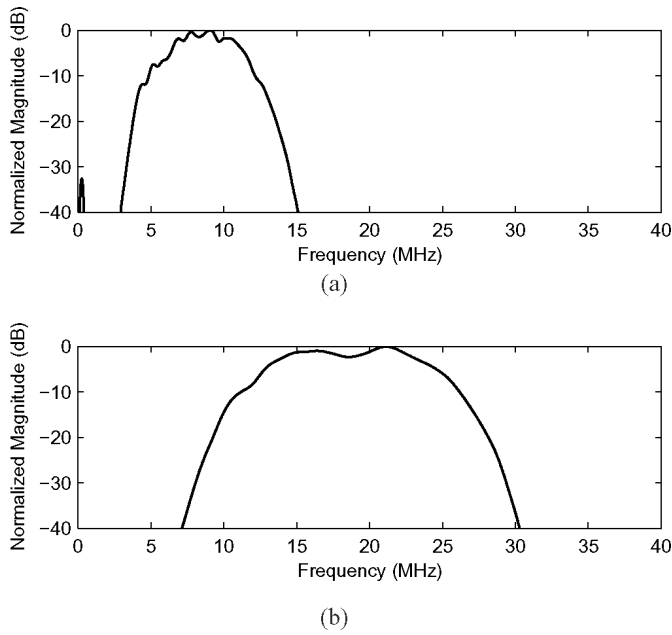$$f_c = (f_{+,6dB} + f_{-,6dB})/2, \qquad (1)$$

(a)

(b)

Fig. 6. FFT of filtered pulse-echo response. (a) Conventional. (b) Collapse mode.

(a)

(b)

Fig. 7. Uniformity across ring array, conventional mode. (a) Center frequency. (b) Fractional bandwidth.

and fractional bandwidth:

$$\Delta f/f = (f_{+,6dB} - f_{-,6dB})/f_c. \tag{2}$$

The results are plotted in Figs. 7 and 8. In conventional mode, the device operates at 8.3 MHz with a 6 dB bandwidth of 5.8 MHz. In collapse mode, it operates at 19 MHz with a bandwidth of 13 MHz. All 64 elements were functional and exhibit excellent uniformity.

B. Image Reconstruction Procedure

A-scans from the 64×64 combinations of transmit-receive channels enable off-line construction of volume data using a variety of schemes. B-scan sectors of a plane and its transverse plane were generated to demonstrate volumetric imaging.

The method of synthetic phased-array image reconstruction involved radio frequency (RF) beamforming on the filtered A-scans, using dynamic focusing on transmit and receive. The delays were calculated based upon the round trip distance from the transmit element to the point on the beam, then to the receive element. The sample from the A-scan corresponding to this delay was weighted and added to the samples from all the other A-scans that correspond to the same point on the beam. This procedure can be expressed [16] as:

$$U(x,y,z) = \sum_{i=1}^{N} \sum_{j=1}^{N} w_{ij} s_{ij}[k_i + k_j], \tag{3}$$

for each point (x,y,z) on the beam, where:

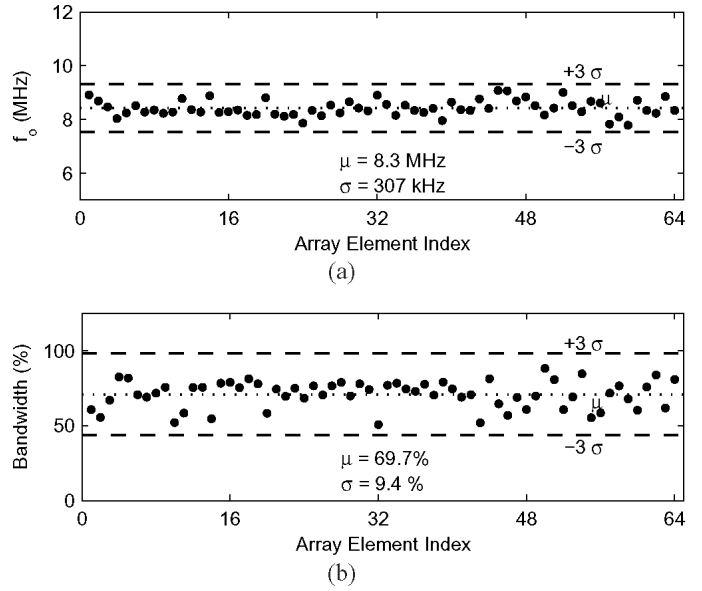$$k_{i,j} = \text{round} \left\{ \frac{f_s}{c} \sqrt{(x-x_{i,j})^2 + (y-y_{i,j})^2 + z^2} \right\}, \tag{4}$$
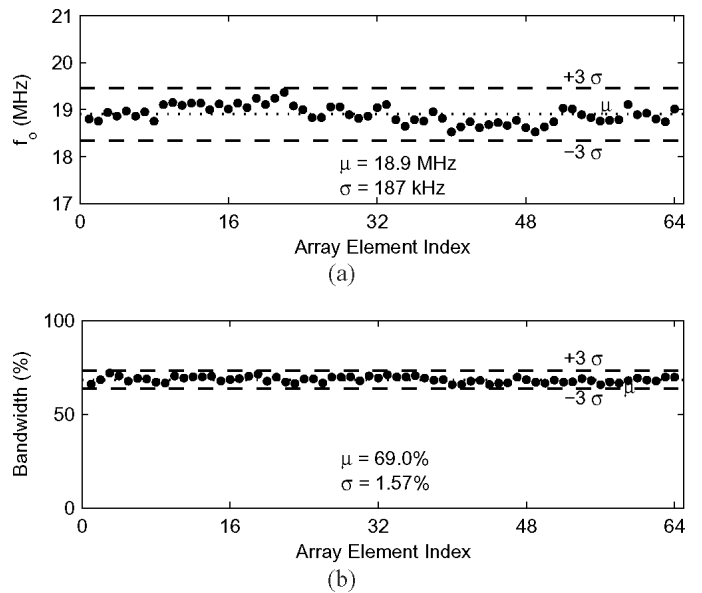

(a)

(b)

Fig. 8. Uniformity across ring array, collapse mode. (a) Center frequency. (b) Fractional bandwidth.

s_{ij} is the A-scan of the ith transmitter and the jth receiver, N is the number of array elements, $(x_i, y_i, 0)$ are the coordinates of the ith element, f_s is the sampling rate, c is the speed of sound, and w_{ij} is the weighting factor:

$$w_{ij} = w_e(i,j)w_n(i,j)w_c(i,j). \tag{5}$$

The array elements were weighted, $w_e(i,j)$, to equalize the signal energy of their pulse-echo responses from the oil-air surface using the A-scan data from the previous section. This compensates for small differences in sensitivity among the elements.

Norton's weightings to obtain full-disk resolution from a ring aperture [2] were applied:

TABLE II
IMAGING PARAMETERS.

Depth of image, mm	9.62
Sector angle, degrees	90
Number of beamlines (Q)	101
Number of points along beamline	660
Pixel size in sector image, μm^2	25×25

TABLE III
SUMMARY OF RESULTS.

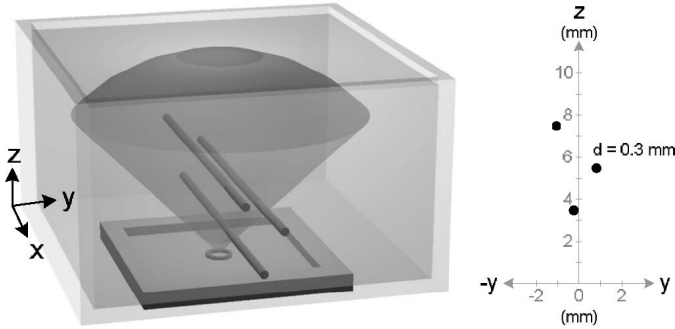|	Conventional	Collapse
Pulse-echo center frequency (f_0), MHz	8.3	19
Pulse-echo fractional bandwidth, %	69.7	69.0
Lateral resolution ($\Delta\theta_{6-dB}$), radians	0.112	0.051
Axial resolution (Δr_{6-dB}), μm	189	78
Wire A-scan SNR, 0 avg (dB)	13	9
Image SNR, 0 avg (dB)	38	34
Wire A-scan SNR, 16 avg (dB)	22	24
Image SNR, 16 avg (dB)	50	48

Fig. 9. Imaging phantom and orientation: three steel wires, 0.3 mm in diameter each.

$$w_n(i,j) = 2|\sin(\theta_i - \theta_j)|, \qquad (6)$$

where θ_i is the angle in the plane of the transducer to the transmit element, and θ_j is the angle to the receive element.

Cosine apodization [17] of the aperture in the radial dimension was applied to suppress sidelobes:

$$w_c(i,j) = \frac{1 + K\cos(\frac{\pi\rho_{i,j}}{2a})}{1 + K}, \qquad (7)$$

where:

$$\rho_{i,j} = a\sqrt{2 + 2\cos(\theta_i - \theta_j)}, \qquad (8)$$

is the radius of the effective aperture, a is the radius of the ring array, and K is a parameter that can be adjusted to trade off between resolution and sidelobe suppression. In this paper, $K = 1$ is chosen.

The beams were envelope detected, scan converted, and logarithmically compressed for display. A 90° field of view was uniformly sampled in $\sin(\theta)$ space with 101 beams. The beams were sampled axially every 12.3 μm. The imaging parameters are summarized in Table II.

C. B-Scan Results

For imaging experiments, a phantom of three steel wires each 0.3 mm in diameter, shown in Fig. 9, was used to characterize the line spread function of the system. This phantom was scanned with 16 and zero averages in both conventional and collapse modes. Fig. 10 shows the Y-Z and X-Z planes of the conical volume, reconstructed from data

averaged 16 times and using $K = 1$. Because of the higher frequency and reduced acoustic cross talk, collapse mode produces images with a narrower main lobe and fewer artifacts than conventional mode imaging. The Y-Z plane clearly shows a cross section of the wires. In the images of the X-Z plane, only the nearest wire appears as a bright line because it is the only one that lies in the plane of this slice.

Image SNR was calculated for the closest wire at 3.5 mm and compared to the average A-scan SNR of the wire. The image signal was found by manually taking a small rectangular kernel about the brightest point corresponding to the wire. The A-scan SNR was found by taking a fixed window about the peak of the pulse that corresponded to the wire and averaging over all 4096 A-scans. This was done for scans taken with 16 and zero averages. Even with no averaging, there still is roughly 35 dB of SNR, which allows strong reflectors such as stents to be easily seen. This is a notable result considering that each element of the ring array is only 100 μm × 100 μm in size.

Table III summarizes the imaging performance of this system for both modes of operation.

D. Reduced Firing Set

Because the hardware and interconnect for a catheter probe will likely be highly limited, a reduced set of transmit and receive combinations is required to keep the frame rate high and suppress motion artifacts. Following the methodology presented in [1], offline beamforming was performed with reduced firing sets to investigate the viability of such a scheme using experimental data from a CMUT ring array. A custom reduced-firing set with 276 transmit-receive combinations was generated for the conventional, 8-MHz operation of the CMUT. A reduced firing set for collapse mode was not made because the frequency (19 MHz) was not suitable for this array design. In the cited work, two adjacent elements were tied together during transmit to increase output power. Here, this was simulated by applying to both elements during beamforming the average delay for these two elements.

The coarray is defined as the convolution of the transmit/receive aperture with itself. The coarray is formed on a point-by-point basis by the vector sum of the transmit and receive elements as illustrated in Fig. 11. A particular
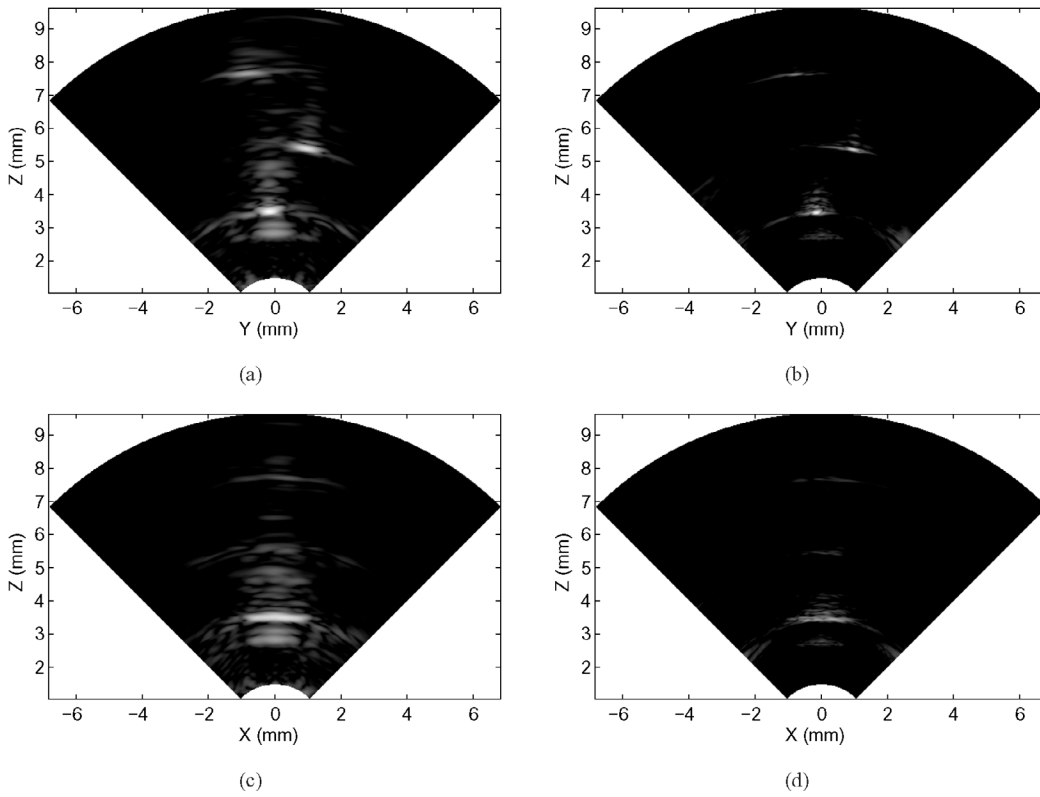
Fig. 10. Slices of 3-D volume, 40 dB range. (a) Y-Z plane, conventional. (b) Y-Z plane, collapse mode. (c) X-Z plane, conventional. (d) X-Z plane, collapse mode.
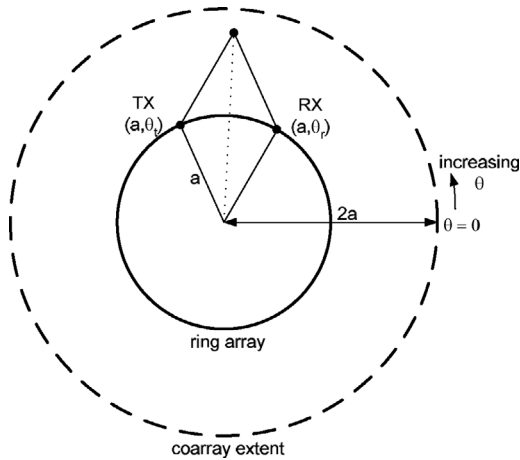

Fig. 11. Schematic of coarray formation.

Fig. 12. Coarray of reduced firing set for conventional mode.

offset between the transmit and receive elements corresponds to a ring on the coarray with a particular radius. A subset of the coarray can be chosen such that acceptable imaging performance is achieved. Specifically, the distance between coarray elements must be maintained to avoid grating lobes.

The firing set is given in Table IV for conventional operation. This corresponds to the coarray graphically depicted in Fig. 12. Rings in the coarray that are needlessly dense are thinned, and adjacent rings are offset to minimize the distance between coarray elements. Here, receive element
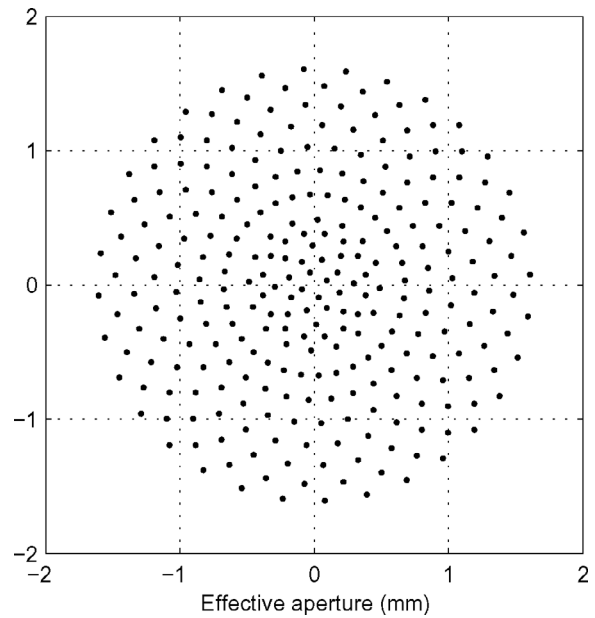
offsets of 13 to 31 are used. Offset 32 is ignored because it contributes only to spatial DC. Offsets smaller than 12 sample the aperture at an intolerably large interval. Offset 13 corresponds to an outer radius of 1.6 mm. Points on this ring of the coarray are an arc length of 315 μm apart. Offset 31 corresponds to an inner radius of 98 μm.
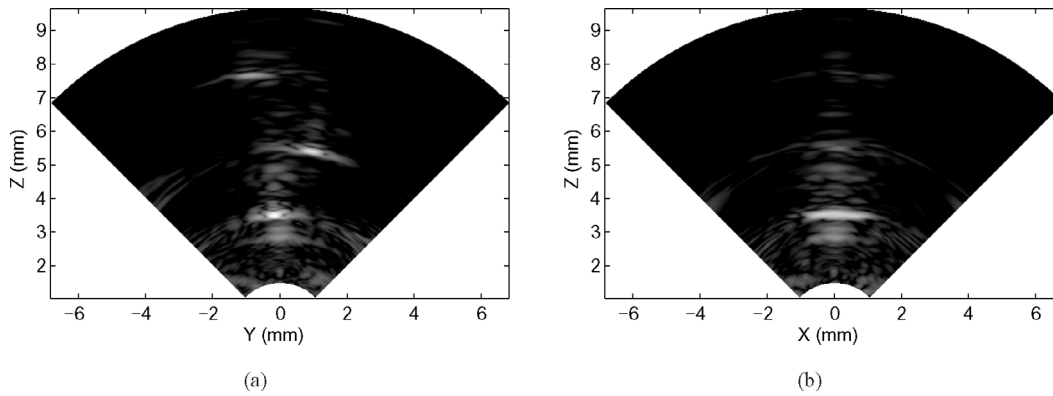
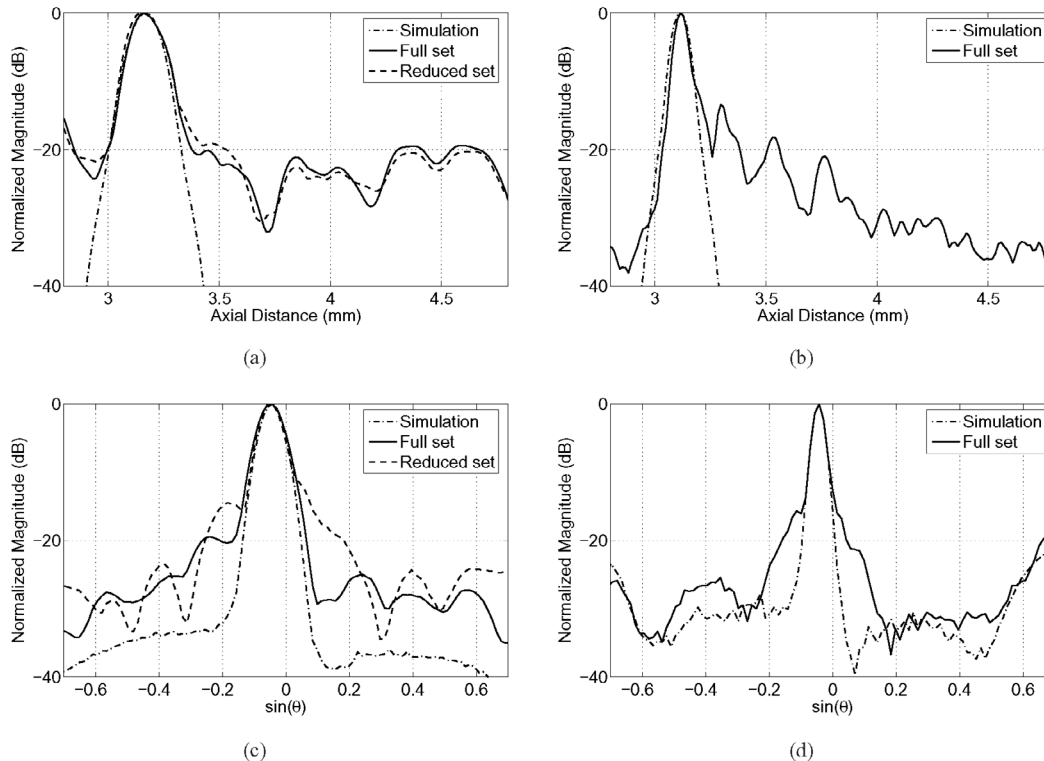Fig. 13. Slices of 3-D volume, 40 dB range, reduced firing set, conventional. (a) Y-Z plane. (b) X-Z plane.

Fig. 14. Line spread functions of nearest wire. (a) Axial LSF, conventional. (b) Axial LSF, collapse mode. (c) Lateral LSF, conventional. (d) Lateral LSF, collapse mode.

TABLE IV
REDUCED FIRING SET FOR CONVENTIONAL OPERATION.

Offset	# Firings
13, 15, ... 25	32
27, 28	16
29, 30	8
31	4

The resulting B-scans are shown in Fig. 13. The images are not much worse than those from the full firing set and demonstrate the viability of using reduced firing sets to implement real-time imaging. The sidelobes are elevated, and grating lobes can now be seen on the second wire because the samples of the coarray are not close enough to keep grating lobes out of the field of view. The samples of the aperture should be one wavelength apart (190 μm at 8 MHz, 79 μm at 19 MHz) to prevent grating lobes. The samples on the outer ring of the coarray are 315 μm apart for the reduced firing case versus 196 μm for the full-firing set.

E. Line Spread Functions

The experimental line spread functions (LSF) are compared to those from simulation in Fig. 14. Simulated data was generated by using Gaussian pulses with the band-
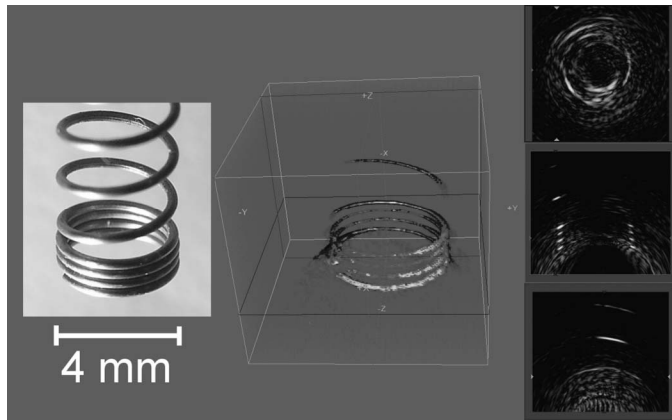
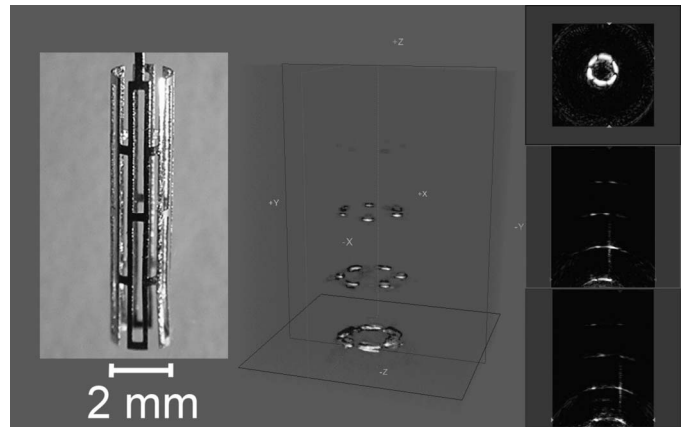Fig. 15. Photograph of spring, 3-D rendered ultrasound image, cross sections with 40 dB dynamic range.

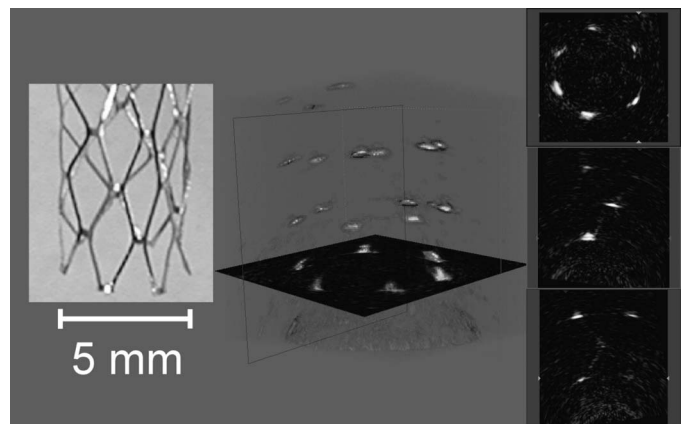Fig. 16. Photograph of Palmaz-Schatz stent, undeployed, 3-D rendered ultrasound image, cross sections with 40 dB dynamic range.

Fig. 17. Photograph of Palmaz-Schatz stent, deployed, 3-D rendered ultrasound image, cross sections with 40 dB dynamic range.

width and center frequency of the CMUT, and with reflectors in the same locations as in the experiment. The axial and lateral LSFs of the system were calculated by averaging 20 lines of pixels in r-sin(θ) space around the line that contained the brightest pixel corresponding to the first wire. Data from the B-scan images with 16 averages and $K = 1$ were used.

In conventional mode, the reduced set provides resolution comparable to that of the full-phased array, although excessive cross talk pollutes the noise floor and prevents an accurate measurement of the lateral LSF. The lateral LSF in collapse mode shows the beginning of grating lobes as explained by the sparse sampling on the coarray. The axial LSF exhibits ringing that is characteristic of cross talk, which is much suppressed relative to conventional mode. Both cases show an excellent match to simulation, especially in terms of main lobe width.

F. Volumetric Imaging

One application of a forward-viewing ring array is to guide stent placement. To demonstrate this, several stent-shaped objects were scanned using 16 averages. The volume was reconstructed directly on a Cartesian grid, using in-phase and quadrature data from the A-scans. The result was rendered and displayed using the volume viewing software, Microview (General Electric Co., London, ON, Canada).

The first is a spring (Fig. 15), 4 mm in diameter, that was taken from a pen. The volume rendered spiral can be seen in the center. A supplemental animation that rotates the rendered spring about the Z-axis has been provided 📹. The three cross sections on the right show the features of the spiral in greater detail, with 40 dB dynamic range. A second animation steps through the cross sections and conveys the structure of the spring 📹.

Next, an undeployed Palmaz-Schatz stent is shown in Fig. 16. The strut planes are strong reflectors and are the prominent features in the rendered image. The C-scan plane shows the bottom opening of the stent. The alternating pattern of the struts and traces of the vertical wall

are visible in the cross sections. The rendered volume is rotated about the Z-axis in the third supplemental animation 📹.

A deployed Palmaz-Schatz stent is shown in Fig. 17. This image is more difficult to interpret due to the sparseness of reflectors. The struts again show up as bright reflectors, which form rungs in the rendered image. The X-shaped patterns that make up the walls of the stent can be seen in the cross sections. The bottom rung is captured in the image of the C-scan plane. The rendered volume is rotated about the Z-axis in the supplemental animation 📹.

These last two images demonstrate that the Palmaz-Schatz stent is clearly visible in both undeployed and deployed states. The extent of the stent can be accurately determined using the ultrasound image. This transducer potentially can locate a stent and confirm deployment.

IV. Conclusions

Synthetic phased-array ultrasound imaging using a forward-viewing CMUT ring array with custom ICs has been demonstrated. Compelling 3-D images of several wire

targets and Palmaz-Schatz stents have been presented, indicating the practical promise of imaging with such a device. It is the high yield of the CMUT fabrication process in combination with the efficacy of the CMUT transduction method and the use of custom-integrated circuits that makes imaging with such small transducer elements possible. A system fully integrated with electronics either monolithically or using flip-chip technology can make use of customized beamforming methods to improve SNR and increase frame rate. Advanced driving circuitry that implements bipolar pulses and coded excitation can contribute to additional gains in SNR. These results and the potential of further improvements point to an auspicious future for forward-viewing CMUT ring arrays in intravascular imaging.

ACKNOWLEDGMENT

REFERENCES

[1] Y. Wang, D. N. Stephens, and M. O'Donnell, "Optimizing the beam pattern of a forward-viewing ring-annular ultrasound array for intravascular imaging," *IEEE Trans. Ultrason., Ferroelect., Freq. Contr.*, vol. 49, no. 12, pp. 1652–1664, Dec. 2002.

[2] S. J. Norton, "Annular array imaging with full-aperture resolution," *J. Acoust. Soc. Amer.*, vol. 92, no. 6, pp. 3202–3206, Dec. 1992.

[3] S. J. Norton, "Synthetic aperture imaging with arrays of arbitrary shape—Part II: The annular array," *IEEE Trans. Ultrason., Ferroelect., Freq. Contr.*, vol. 49, no. 4, pp. 404–408, Apr. 2002.

[4] J. Crowe, J. Hamilton, D. Stephens, Y. Wang, and M. O'Donnell, "Modified weighting method for forward-looking ring-annular arrays," *Ultrason. Imag.*, vol. 23, pp. 19–38, 2001.

[5] Y. Wang, D. N. Stephens, and M. O'Donnell, "Initial results from a forward-viewing ring-annular ultrasound array for intravascular imaging," in *Proc. IEEE Ultrason. Symp.*, 2003, pp. 212–215.

[6] A. Ergun, Y. Huang, C.-H. Cheng, Ö. Oralkan, J. Johnson, H. Jagannathan, U. Demirci, G. Yaralioglu, M. Karaman, and B. Khuri-Yakub, "Broadband capacitive micromachined ultrasonic transducers ranging from 10 kHz to 60 MHz for imaging arrays and more," in *Proc. IEEE Ultrason. Symp.*, 2002, pp. 1039–1043.

[7] U. Demirci, A. S. Ergun, Ö. Oralkan, M. Karaman, and B. T. Khuri-Yakub, "Forward-viewing CMUT arrays for medical imaging," *IEEE Trans. Ultrason., Ferroelect., Freq. Contr.*, vol. 51, no. 7, pp. 887–895, July 2004.

[8] Ö. Oralkan, S. Hansen, B. Bayram, G. Yaralioglu, A. Ergun, and B. Khuri-Yakub, "CMUT ring arrays for forward-looking intravascular imaging," in *Proc. IEEE Ultrason. Symp.*, 2004, pp. 403–406.

[9] D. T. Yeh, Ö. Oralkan, A. S. Ergun, X. Zhuang, I. O. Wygant, and B. T. Khuri-Yakub, "High-frequency CMUT arrays for high-resolution medical imaging," in *Proc. SPIE Med. Imaging 2005: Ultrason. Imaging Signal Processing*, vol. 5750, San Diego, CA, 2005, pp. 87–98.

[10] J. Knight, J. McLean, and F. L. Degertekin, "Low temperature fabrication of immersion capacitive micromachined ultrasonic transducers on silicon and dielectric substrates," *IEEE Trans. Ultrason., Ferroelect., Freq. Contr.*, vol. 51, no. 10, pp. 1324–1333, Oct. 2004.

[11] F. L. Degertekin, R. O. Guldiken, and M. Karaman, "Micromachined capacitive transducer arrays for intravascular ultrasound," in *Proc. SPIE MOEMS Display and Imaging Systems III*, vol. 5721, no. 1, San Jose, CA, 2005, pp. 104–114.

[12] Ö. Oralkan, A. S. Ergun, J. A. Johnson, U. Demirci, M. Karaman, K. Kaviani, T. H. Lee, and B. T. Khuri-Yakub, "Capacitive micromachined ultrasonic transducers: Next-generation arrays for acoustic imaging?," *IEEE Trans. Ultrason., Ferroelect., Freq. Contr.*, vol. 49, no. 11, pp. 1596–1610, Nov. 2002.

[13] B. Bayram, E. Hæggström, G. G. Yaralioglu, and B. T. Khuri-Yakub, "A new regime for operating capacitive micromachined ultrasonic transducers," *IEEE Trans. Ultrason., Ferroelect., Freq. Contr.*, vol. 50, no. 9, pp. 1184–1190, Sep. 2003.

[14] G. S. Kino, *Acoustic Waves: Devices, Imaging, and Analog Signal Processing.* Englewood Cliffs, NJ: Prentice-Hall, 1987.

[15] B. Bayram, M. Kupnik, G. G. Yaralioglu, Ö. Oralkan, D. Lin, X. Zhuang, A. S. Ergun, A. F. Sarioglu, S. H. Wong, and B. T. Khuri-Yakub, "Characterization of cross-coupling in capacitive micromachined ultrasonic transducers," presented at IEEE Int. Ultras. Symp., Rotterdam, The Netherlands, Sep. 18–21, 2005.

[16] L. Busse and D. Dietz, "Sparse circular array methods, performance, and application to intravascular imaging," in *Proc. IEEE Ultrason. Symp.*, 1991, pp. 641–644.

[17] S. S. Brunke and G. R. Lockwood, "Broad-bandwidth radiation patterns of sparse two-dimensional vernier arrays," *IEEE Trans. Ultrason., Ferroelect., Freq. Contr.*, vol. 44, no. 5, pp. 1101–1109, Sep. 1997.
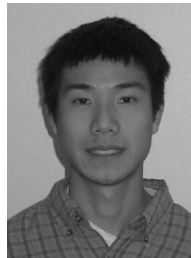
David T. Yeh (S'98) received the B.S. degree in electrical engineering from the University of California at Berkeley in 2002, and the M.S. degree from Stanford University, Stanford, CA, in 2004. He is currently pursuing a Ph.D. degree in electrical engineering at Stanford.

He has previously worked as an undergraduate researcher in the Berkeley Sensor and Actuator Center from 2000 to 2002 in MEMS research. In the summer of 2002 he worked at Hewlett-Packard Labs in Palo Alto, CA, characterizing devices for a roll-to-roll manufacturing process. In the summer of 2003 he performed research at National Semiconductor in Santa Clara, CA on DC-DC power converters. From 2003 to 2005 he has been a graduate student in the Khuri-Yakub Ultrasonics Group at Stanford University. Currently, he is a Ph.D. candidate in the Center for Computer Research in Music and Acoustics at Stanford University.

David is a member of IEEE. He was a student paper finalist at the 2005 Ultrasonics Symposium and is a recipient of the NDSEG and NSF graduate fellowships.

Ömer Oralkan (S'93–M'05) received the B.S. degree from Bilkent University, Ankara, Turkey, in 1995, the M.S. degree from Clemson University, Clemson, SC, in 1997, and the Ph.D. degree from Stanford University, Stanford, CA, in 2004, all in electrical engineering.

Currently, he is an engineering research associate at the Edward L. Ginzton Laboratory at Stanford University. His past and present research interests include analog and digital circuit design, micromachined sensors and actuators, and semiconductor device physics and fabrication. His current research focuses on the design and implementation of integrated ultrasonic imaging systems.

Dr. Oralkan received the 2002 Outstanding Paper Award of the IEEE Ultrasonics, Ferroelectrics, and Frequency Control Society. He is a member of the IEEE.

Ira O. Wygant received his B.S. degree in electrical engineering with a cross-college major in computer science from the University of Wyoming, Laramie, WY, in 1999. He received his M.S. degree in electrical engineering from Stanford University, Stanford, CA, in 2002. He is currently pursuing a Ph.D. degree in electrical engineering at Stanford University.

Ira has held internships in the mixed-signal and monolithic sensors group at Oak Ridge National Laboratory, Oak Ridge, TN, in a wireless RF IC design group at Lucent Technologies, Reading, PA, and in the mixed-signal electronics group at Agilent Laboratories, Palo Alto, CA. His research interests include IC and system design for ultrasound imaging systems based on capacitive micromachined ultrasonic transducers (CMUTs). Ira was the recipient of a National Science Foundation Graduate Research Fellowship.

Matthew O'Donnell (M'79–SM'84–F'93) received the B.S. and Ph.D. in Physics, University of Notre Dame, Notre Dame, IN, in 1972 and 1976, respectively.

Following his graduate work, Dr. O'Donnell moved to Washington University in St. Louis, MO as a postdoctoral fellow in the Physics Department working on applications of ultrasonics to medicine and nondestructive testing. He subsequently held a joint appointment as a Senior Research Associate in the Physics Department and a Research Instructor of Medicine in the Department of Medicine at Washington University. In 1980 he moved to General Electric Corporate Research and Development Center in Schenectady, NY, where he continued to work on medical electronics, including MRI and ultrasound imaging systems. During the 1984–1985 academic year, he was a visiting fellow in the Department of Electrical Engineering at Yale University in New Haven, CT investigating automated image analysis systems. In a bold move during 1990, Dr. O'Donnell became a Professor of Electrical Engineering and Computer Science at the University of Michigan in Ann Arbor, MI. Since 1997, he has held a joint appointment as Professor of Biomedical Engineering at Michigan, and in 1998 he was named the Jerry W. and Carol L. Levin Professor of Engineering. Currently, he is the Chair of the Biomedical Engineering Department. His most recent work has explored new imaging modalities in biomedicine, including elasticity imaging, *in vivo* microscopy, optoacoustic arrays, optoacoustic contrast agents for molecular imaging and therapy, thermal strain imaging, and catheter based devices.

Butrus T. Khuri-Yakub (S'70–S'73–M'76–SM'87–F'95) was born in Beirut, Lebanon. He received the B.S. degree in 1970 from the American University of Beirut, the M.S. degree in 1972 from Dartmouth College, and the Ph.D. degree in 1975 from Stanford University, all in electrical engineering. He joined the research staff at the E. L. Ginzton Laboratory of Stanford University in 1976 as a research associate. He was promoted to senior research associate in 1978, and to a Professor of Electrical Engineering (Research) in 1982. He has served on many university committees in the School of Engineering and the Department of Electrical Engineering.

Presently, he is the Deputy Director of the E. L. Ginzton Laboratory, and the associate chairman for graduate admissions in the electrical engineering department at Stanford. Professor Khuri-Yakub has been teaching both at the graduate and undergraduate levels for over 20 years, and his current research interests include in situ acoustic sensors (temperature, film thickness, resist cure, etc.) for monitoring and control of integrated circuits manufacturing processes, micromachining silicon to make acoustic materials and devices such as airborne and water immersion ultrasonic transducers and arrays, and fluid ejectors, and in the field of ultrasonic nondestructive evaluation and acoustic imaging and microscopy.

Professor Khuri-Yakub is a fellow of the IEEE, a senior member of the Acoustical Society of America, and a member of Tau Beta Pi. He is associate editor of Research in Nondestructive Evaluation, a Journal of the American Society for Nondestructive Testing. Professor Khuri-Yakub has authored over 400 publications and has been principal inventor or co-inventor of 60 issued patents. He received the Stanford University School of Engineering Distinguished Advisor Award, June 1987, and the Medal of the City of Bordeaux for contributions to NDE, 1983.